

Supplemental to “The development of internal pressure standards for in-house elastic wave velocity measurements in multi-anvil presses”

A. Néri^{1,&,*}, L. Man¹, J. Chantel², R. Farla³, G. Bauer¹, S. Linhardt¹, T. Boffa Ballaran¹ and D.J. Frost¹

¹ Bayerisches Geoinstitut, University of Bayreuth, Bayreuth, Germany

² Université de Lille, CNRS, INRAE, Centrale Lille, UMR 8207 - UMET - Unité Matériaux et Transformations, F-59000 Lille, France

³ Deutsches Elektronen-Synchrotron DESY, Hamburg, Germany

& Now at Université de Lille, CNRS, INRAE, Centrale Lille, UMR 8207 - UMET - Unité Matériaux et Transformations, F-59000 Lille, France

*Corresponding author, e-mail address: adrien.neri@univ-lille.fr

S.1 Frequency effect on the P-wave travel time

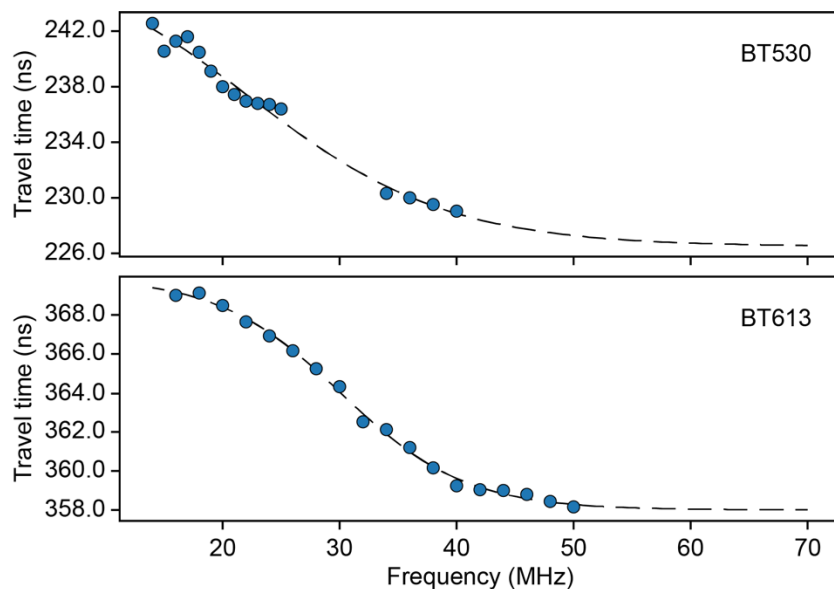


Figure S.1: Effect of frequency on the two-way travel of P-waves between BT530 and BT613; the dashed line shows an arbitrary sigmoid fit as a guide for the eye. The limited accessible frequency range of data collection during BT530 yields an overestimation of the travel time, thus an underestimation of the P-wave velocities. On the other hand, the frequency range sampled during BT613 is large enough to give the appropriate P-wave velocities.

Due to the mismatch between the measured and predicted P-wave velocities (Fig. 4c), the frequency dependence of the P-wave travel times has been investigated. Fig. S.1 shows the evolution of travel times as a function of frequency for the last data point collected during BT530 and BT613. The last data point collected was chosen as the F_{90} samples have been annealed for several hours and to peak temperatures exceeding 1273 K, preventing these samples from exhibiting any residual stress. Even in a fully relaxed state, for both BT530 and BT613, the travel times show a frequency dependence. More importantly, BT613 shows a plateau at high frequencies (> 40 MHz), where travel times are not dependent on the frequency anymore. Due to its large size (6.35 mm in diameter), the piezoelectric crystal used during the experiment BT530 was unable to produce a signal where echoes could be correlated for frequencies larger than 40 MHz. Thus, the P-wave travel times measured during BT530 could not show the same plateau as BT613 (dashed lines are a guide for the eye corresponding to a sigmoid fit), yielding P-wave velocity values that are underestimated (as seen in Fig. 4c).

Conducting a similar exercise on S-wave travel times shows a similar travel time dependence on the frequency, but with a plateau that appears for frequencies larger than 34 MHz. Data could be collected well within this range for both experiments BT530 and BT613. Interestingly, both threshold frequencies to reach the travel time plateau correspond to the resonance frequencies of 63 μm thick LiNbO₃ piezoelectric crystals.

When only the high-frequency ranges are considered to calculate P-wave and S-wave velocities, the obtained room temperature values are in perfect agreement with room temperature Brillouin data (Abramson et al., 1997; Mao et al., 2015; Zha et al., 1998; Zhang and Bass, 2016). As such, only these high-frequency data were used to report elastic wave velocities in Table S.2 and considered during the fit of our EoS.

This description highlights the critical need for high-quality and small piezoelectric crystals to collect high-quality travel time data and estimate reliable elastic wave velocity values. If transducers cannot reach the frequency thresholds to reach the P- and S-wave travel time plateaus, then the determined P- and S-wave velocity values can be underestimated as in the case of BT530.

S.2 Derivation of the near field length

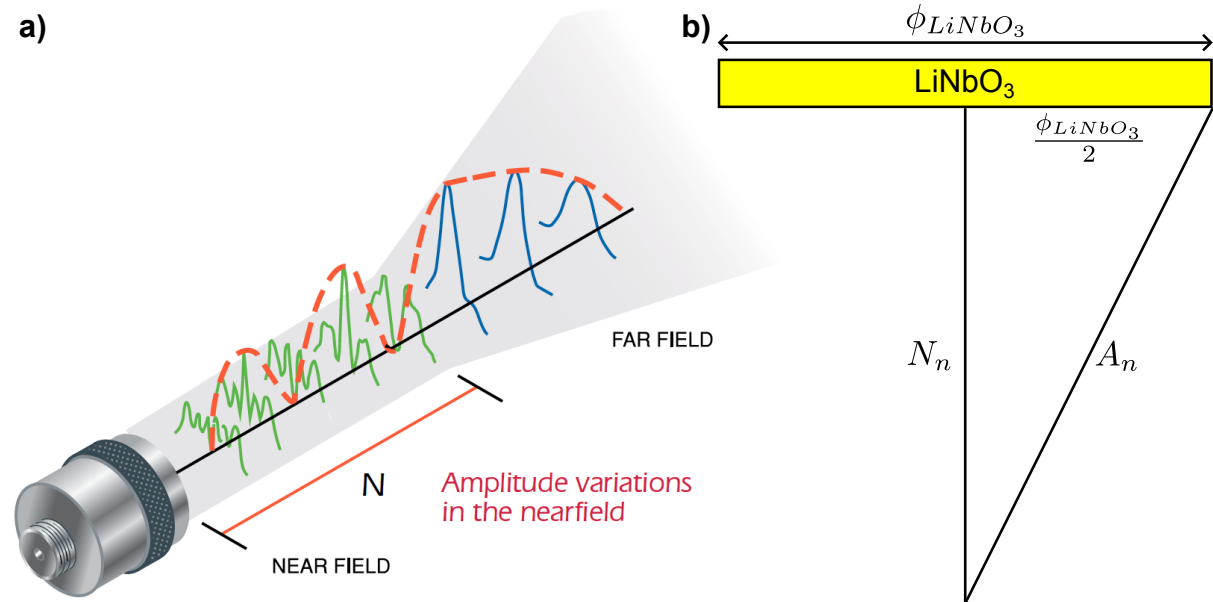


Figure S.2: (a) Schematic representation of the acoustic pressure profile showing the series of minima and maxima within the near field (taken from the Olympus Ultrasonic Transducers Technical Notes, <https://www.olympus-ims.com/en/ndt-tutorials/transducers/characteristics/>). (b) Geometrical sketch showing the dimensions used to calculate the near field distance.

The acoustic pressure profile is often divided into two areas. The first one, close to the source is called the near field and is characterized by a series of pressure minima and pressure maxima (Fig. S.2a). The last maximum delimits the near field from the far field and represents the natural focus of the transducer. The minima are produced from destructive interferences between the signal generated at the point center of the transducer and its edge. The distance between the transducer and the acoustic pressure minima can be expressed by considering the condition for wave interference. Wave interferences occur when the phase difference is equal to π , i.e. when the path difference Δd between two rays of wavelength λ is:

$$\Delta d = \left(n + \frac{1}{2}\right)\lambda. \quad (\text{S.1})$$

By geometrical construction (see Fig. S.2b), let us consider N_n the path-distance of a ray generated at the center transducer and the n^{th} acoustic pressure minima, and A_n the path-distance of a ray generated at the edge of the transducer and the n^{th} acoustic pressure minima. Then, the path difference between these two rays is:

$$\Delta d = \left(n + \frac{1}{2}\right)\lambda = A_n - N_n. \quad (\text{S.2})$$

Using Pythagoras' theorem, we can express A_n as a function of N_n and ϕ_{LiNbO_3} the transducer diameter such that:

$$A_n^2 = N_n^2 + \frac{\phi_{LiNbO_3}^2}{4}. \quad (\text{S.3})$$

By combining equations (S.2) and (S.3), N_n is expressed as a function of the transducer diameter and of the wavelength:

$$N_n = \frac{\phi_{LiNbO_3}^2}{4(2n+1)\lambda} - \left(n + \frac{1}{2}\right) \frac{\lambda}{2}. \quad (\text{S.4})$$

Considering the wavelength at a given frequency, $\lambda = \frac{v_p}{f}$, where v_p is the velocity within the material of interest and f the frequency, equation (S.4) can be expressed as a function of frequency, yielding:

$$N = \frac{\phi_{LiNbO_3}^2 f}{4v_p(2n+1)} - \left(n + \frac{1}{2}\right) \frac{v_p}{2f}. \quad (\text{S.5})$$

Here, the frequency range of interest corresponds to the mega-Hertz, meaning that the term $\left(n + \frac{1}{2}\right) \frac{v_p}{2f}$ is very small and thus often neglected, giving the final expression used here:

$$N = \frac{\phi_{LiNbO_3}^2 f}{4v_p(2n+1)}. \quad (\text{S.6})$$

The last destructive interference used to separate the near field from the far field corresponds to the condition $n = 0$, simplifying equation (S.6) to:

$$N = \frac{\phi_{LiNbO_3}^2 f}{4v_p}. \quad (\text{S.7})$$

S.3 Sample synthesis

San Carlos-like olivine ($Mg / (Mg + Fe) = 0.9$ in moles) was synthesized by mixing reagent grade oxides (MgO 99.99%, SiO_2 99.9% and Fe_2O_3 99.9%, all from Chempur) in the appropriate proportions (40.43 wt.% SiO_2 , 48.82 wt.% MgO and 10.75 wt.% Fe_2O_3). The MgO and SiO_2 powders were dried at 1273 K overnight prior to mixing to remove the adsorbed water. Batches of 4 g were prepared at once to minimize the weighing uncertainties on each species. After mixing, the powders were reacted and reduced ($\Delta FMQ = -2$) in a CO_2/CO gas mixing furnace at 1373 K overnight (≈ 16 hours). This process was repeated twice with mechanical grinding and mixing in between, using an agate mortar, to ensure chemical homogeneity and complete reactions. The recovered starting material was then checked using a powder diffractometer to ensure that no residual starting products remained and to determine the unit cell volume (see Supplementary Material S.4).

Small batches of San Carlos-like olivine powder were then crushed in an agate mortar and under ethanol for one hour, to ensure that the initial grain size is small ($\approx 6-8 \mu m$). The fine-grained powder was then enclosed in a sealed platinum capsule and sintered using a piston-cylinder 3/4-inch standard BGI assembly (Keppler and Frost, 2005), at conditions of 0.7 GPa and 1373 K maintained for 2 h. The temperature was quenched by shutting off the power supply, and decompression was made as slow as possible to avoid cracks, i.e. over 8 to 15 hours. The recovered sintered blocks were machined into double-side mirror-grade polished disks of 2.5 mm diameter and 1.2 to 1.5 mm height.

S.4 X-ray diffraction data collection and analysis

The purity of the synthetic San Carlos-like olivine was checked using a Philips X'Pert Pro X-ray diffraction system operating in reflection mode, with $CoK\alpha 1$ ($\lambda = 1.78897 \text{ \AA}$) radiation selected with a focusing monochromator, a symmetrically cut curved Johansson $Ge(111)$ crystal and a Philips X'celerator detector. The X-ray tube was tuned to 40 kV and 40 nA, while collection times in the 2θ range of 10-100° were fixed to 100 s for each step. Prior to the analysis, the powder was mixed with a NIST silicon standard ($a = 5.43119 \text{ \AA}$) to correct for the source offset. Data were analyzed using GSAS-II (Toby and Von Dreele, 2013) and none of the starting oxides were observed on the diffraction pattern. A Le Bail fit was conducted to refine the unit cell parameters, which were found to be $a = 4.76206(30) \text{ \AA}$, $b = 10.22344(52) \text{ \AA}$, and $c = 5.99302(34) \text{ \AA}$, yielding a unit cell volume of $291.768(18) \text{ \AA}^3$.

Energy dispersive X-ray diffraction patterns were collected during the experiments on P61B. The beamline features two high-purity germanium solid-state detectors (Ge-SSD) by Mirion (Canberra). The 2θ diffraction angle was calibrated for each experiment from the known unit cell parameters of materials present within the assembly. A mixture of $MgO + Pt$ (MgO 99.99% 1.5 μm , Pt 99.95+% 0.2-1.8 μm from Chempur) was inserted in the assembly to constitute the pressure standards to be used on the X-ray diffraction. Platinum is mostly used to hinder the grain growth of MgO at high temperatures; due to its

softness, since Pt acquires very easily a preferred orientation and can hardly be used as a pressure standard. For BT530, the MgO and Pt calibrants were inserted in a groove within the MgO sleeve surrounding the sample and could never be found. Thus, the diffraction angle was calibrated against the unit cell parameters of the synthetic San Carlos-like olivine used as the sample and yielded $2\theta = 3.991^\circ$ and the alumina backing plate was used as the pressure standard. For the BT613 experiment, the MgO and Pt mixture was pressed into a small pellet that was inserted at the back of the backing plate. Thus, the 2θ angle could be calibrated against the unit cell parameters of MgO ($a = 4.211 \text{ \AA}$ for a unit cell volume of 74.672 \AA^3 , and yielded $2\theta = 5.963^\circ$.

For the collection of each XRD pattern, the press was rotated within $\pm 3^\circ$ to increase grain statistics, and the collection time was set to 100 s. The unit cell volumes of each material were obtained using Le Bail refinements in GSAS-II (Toby and Von Dreele, 2013). Due to the presence of lead parts in the optics along the beam path, two main lead fluorescence peaks were observed within the energy-dispersive XRD patterns: $K\alpha_1$ at 74.97 keV and $K\alpha_2$ at 72.81 keV. Thus, care was taken to exclude the range 71–76 keV so that these fluorescence peaks do not affect the unit cell refinement. For BT530 in which a rhenium heater was used, the Re $K\alpha_1$ at 61.14 keV and $K\alpha_2$ at 59.72 keV emission lines could also be observed on the diffraction patterns, thus the range 58–63 keV was also excluded. All unit cell volumes are reported in [Table S.2](#).

The pressure was estimated from the unit cell volumes of MgO and Al_2O_3 determined from the X-ray diffraction data. The equations of state, EoS, reported by (Tange et al. 2009) was used for MgO, while a fit was conducted on the available literature data (D'Amour et al., 1978; Dewaele and Torrent, 2013; Fiquet et al., 1999; Higo et al., 2018; Shi et al., 2022) to refine the P-V-T equation of state of α -alumina ([see Supplementary Material sections S.5 and S.6](#) for more details).

S.5 Mie-Grüneisen-Debye equation of state

For the analysis of the high-pressure high-temperature data, the thermal equation of state description of (Stixrude and Lithgow-Bertelli 2005) was adopted. In this formalism, the total pressure corresponds to the sum of the isothermal pressure $P(V, T_0)$ at a reference temperature $T_0 = 300 \text{ K}$, and a thermal pressure $\Delta P_{th}(V, T)$, following:

$$P(V, T) = P(V, T_0) + \Delta P_{th}(V, T). \quad (\text{S.8})$$

The isothermal pressure, $P(V, T_0)$, is expressed following the third-order Birch-Murnaghan equation of state (Birch, 1952):

$$P(V, T_0) = 3 K_{T_0} f (1 + 2f)^{5/2} \left[1 + \frac{3}{2} (K' - 4)f \right]. \quad (\text{S.9})$$

where K_{T_0} is the isothermal bulk modulus, K' its pressure derivative and f is expressed as:

$$f = \frac{1}{2} \left[\left(\frac{V_0}{V} \right)^{2/3} - 1 \right], \quad (\text{S.10})$$

with V the molar volume at pressure and V_0 the molar volume at a pressure of 10^4 GPa and at the reference temperature. The thermal pressure can then be described as follows:

$$\Delta P_{th}(V, T) = \frac{\gamma}{V} [E_{th}(V, T) - E_{th}(V, T_0)], \quad (\text{S.11})$$

where γ is the Grüneisen parameter, $E_{th}(V, T)$ and $E_{th}(V, T_0)$ are the thermal energies at high temperature and at the reference temperature. The thermal energy can be expressed as:

$$E_{th}(V, T) = 9nRT \left(\frac{\theta}{T} \right)^{-3} \int_0^{\theta/T} \frac{x^3}{e^x - 1} dx, \quad (\text{S.12})$$

where n is the number of atoms per formula unit (5 for corundum, 7 for olivine, and 2 for periclase), R the ideal gas constant, and θ is the Debye temperature. Both the Grüneisen parameter and the Debye temperature can be expressed as follows:

$$\gamma = \frac{1}{6} \frac{v_0^2}{v^2} (2f + 1) [a_{ii} + a_{iikk} f], \quad (\text{S.13})$$

$$\theta = \theta_0 \left(1 + a_{ii} f + \frac{1}{2} a_{iikk} f^2 \right)^{1/2}, \quad (\text{S.14})$$

with:

$$\frac{v^2}{v_0^2} = 1 + a_{ii} f + \frac{1}{2} a_{iikk} f^2, \quad (\text{S.15})$$

$$a_{ii} = 6\gamma_0, \quad (\text{S.16})$$

$$a_{iikk} = -12\gamma_0 + 36\gamma_0^2 - 18q_0\gamma_0. \quad (\text{S.17})$$

γ_0 and θ_0 correspond to the Grüneisen parameter and the Debye temperature at the reference temperature. q_0 is the volume derivative of the Grüneisen parameter, also at the reference temperature.

In turn, the isothermal bulk modulus and the shear modulus are evaluated at pressure and temperature following:

$$K_T = (1 + 2f)^{5/2} \left[K_{T0} + (3K_{T0}K' - 5K_{T0})f + \frac{27}{2}(K_{T0}K' - 4K_{T0})f^2 \right] + (\gamma + 1 - q) \frac{\gamma}{v} [E_{th}(V, T) - E_{th}(V, T_0)] - \frac{\gamma^2}{v} [TC_V(V, T) - T_0C_V(V, T_0)], \quad (\text{S.18})$$

and,

$$G = (1 + 2f)^{5/2} \left[G_0 + (3K_{T0}G' - 5G_0)f + \left(6K_{T0}G' - 24K_{T0} - 14G_0 + \frac{9}{2}K_{T0}K' \right) f^2 \right] - \frac{\eta_S}{v} [E_{th}(V, T) - E_{th}(V, T_0)]. \quad (\text{S.19})$$

Here, G' denotes the pressure derivative of the shear modulus. The volume derivative of the Grüneisen parameter, q , at pressure and temperature can be expressed as:

$$\gamma q = \frac{1}{9} \left[18\gamma^2 - 6\gamma - \frac{1}{2} \frac{v_0^2}{v^2} (2f + 1)^2 a_{iikk} \right]. \quad (\text{S.20})$$

The shear strain derivative of the Grüneisen parameter, η_S , follows:

$$\eta_S = -\gamma - \frac{1}{2} \frac{v_0^2}{v^2} (2f + 1)^2 a_S, \quad (\text{S.21})$$

with the coefficient a_S expressed as a function of the reference temperature Grüneisen parameter γ_0 and its shear strain derivative η_{S0} :

$$a_S = -2\gamma_0 - 2\eta_{S0}. \quad (\text{S.22})$$

Finally, the specific heat capacity $C_V(V, T)$ is expressed as follows:

$$C_V(V, T) = 9nR \left(\frac{\theta}{T} \right)^{-3} \int_0^{\theta/T} \frac{x^4 e^x}{(e^x - 1)^2} dx. \quad (\text{S.23})$$

The P- and S-wave velocities, respectively v_P and v_S , correspond to:

$$v_P = \sqrt{\frac{K_S + 4/3G}{\rho}}, \quad (\text{S.24})$$

$$v_S = \sqrt{\frac{G}{\rho}}, \quad (\text{S.25})$$

with ρ the density. Note here that v_P depends on the adiabatic bulk modulus K_S , which requires the additional transformation from isothermal to adiabatic:

$$K_S = K_T + \frac{\gamma^2}{V} T C_V(V, T). \quad (\text{S.26})$$

S.6 Fitting a P-V-T equation of state of corundum from literature data

For more than 40 years, there have been a number of experimental and theoretical studies that investigated the thermoelastic properties of alumina. Although the luminescence of ruby is one of the most well-calibrated pressure gauges in diamond anvil cells, the thermoelastic parameters of corundum are still controversial. Indeed, it is proposed that the bulk modulus and its pressure derivative have either high values (≈ 255 - 260 GPa and ≈ 5) or low values (≈ 245 - 250 GPa and ≈ 4). Interestingly, published studies only compare their fit parameters with already reported ones, and a global fit of all the available experimental data has not been proposed yet. As such, we propose here to do so. Pressure, temperature, and volume data were taken from: (D'Amour et al. 1978; Dewaele and Torrent 2013; Fiquet et al. 1999; Higo et al. 2018; Shi et al. 2022). Unfortunately, the original data from (Dubrovinsky et al. 1998) are reported only in figures and thus are not included. The data collected by (Richet et al. 1988) were not included as they seem to deviate from the rest of the literature data, even when normalized to the volume at ambient conditions (Fig. S.3a, orange crosses).

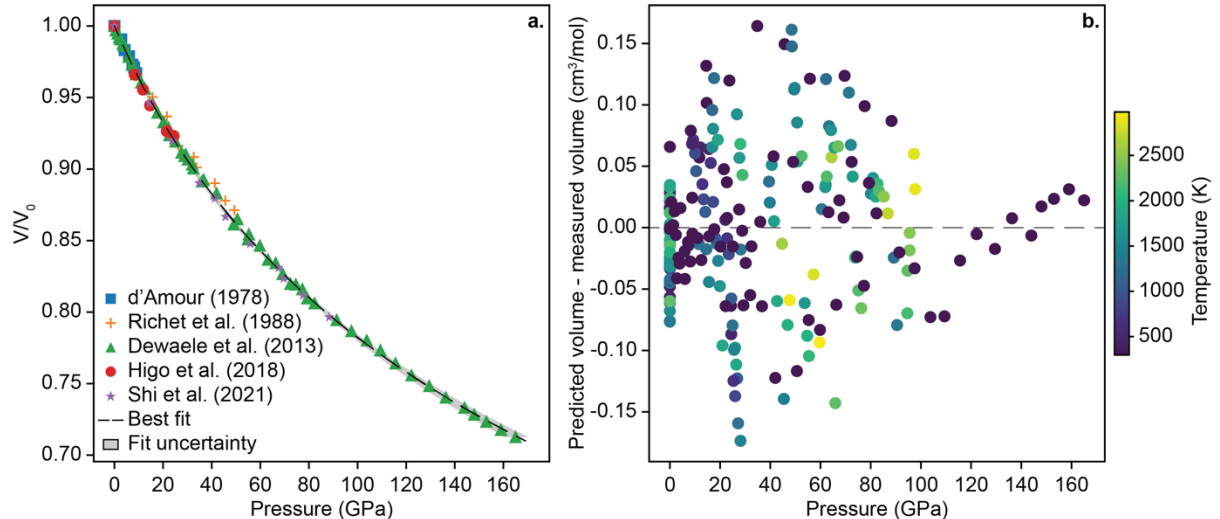


Figure S.3: (a) Normalized volume as a function of pressure for the different datasets considered for our fit. Note that the data from (Richet et al. 1988) have not been used in the fitting procedure. The black line and thin dashed lines show the third-order Birch-Murnaghan fit and associated fit uncertainty. (b) Evaluation of the fit quality is determined as the difference between the measured and predicted unit cell volumes, as a function of pressure and temperature. Overall, the point scatter remains within an envelope of $\approx 1\%$ of the unit cell volume.

First, the room temperature data were fitted using the third-order Birch-Murnaghan equation of state (eq. S.9 and S.10) to extract the isothermal bulk modulus K_{T_0} and its pressure derivative K' . To reduce the variability between the different datasets, the fit was conducted on the normalized molar volumes V/V_0 . A weighted least-squares minimization was conducted using the *curvefit* function from the *Scipy Python* library. A wrapper function was added so that the least-square fit is conducted on the normalized molar volume, by minimizing the misfit in between the measured V/V_0 and the predicted V/V_0 . This way, the least-squares are weighed based on the ratio V/V_0 , which corresponds to the property that is measured during the experiment. When uncertainties were not reported (Dewaele and Torrent 2013; Higo et al. 2018), a constant value of 0.5 \AA^3 was assumed (corresponding to $0.0522 \text{ cm}^3 \cdot \text{mol}^{-1}$). A non-

weighed least-squares fit would return values that overlap within uncertainties: $K_{T0} = 250.5 \pm 3.1$ GPa and $K' = 3.95 \pm 0.1$.

The obtained parameters are: $K_{T0} = 249.7 \pm 3.2$ GPa and $K' = 3.97 \pm 0.1$; uncertainties correspond to two standard deviations extracted from the diagonal of the covariance matrix. To make sure that the values returned by our fitting procedure are correct, it was benchmarked against each dataset. The obtained parameters overlap with those reported in the literature within fitting uncertainties.

The isothermal bulk modulus and its pressure derivative were then fixed, and the Grüneisen parameter γ_0 and its volume derivative q_0 were obtained by fitting the high-temperature data to equations S.8 to S.17. The *integrate* function from the *Scipy Python* library was used to numerically calculate the integral involved in equation S.12. The same method was used as for room temperature data. Here also, V_0 was taken as a variable in between the different datasets to reduce the inter-studies variability. The Debye temperature at T_0 , i.e. θ_0 , was fixed to 933 K, as suggested by (Stixrude and Lithgow-Bertelloni 2005). Interestingly, changing θ_0 to 1100 K, as used in (Shi et al. 2022), yields similar fit parameters, within uncertainties. Here, our fitting procedure was benchmarked against the individual dataset of (Shi et al. 2022). To adopt the same equations as the authors, equations S.13 and S.14 were respectively changed to equations S.27 and S.28. The values of γ_0 and q_0 obtained with our fitting procedure overlap within uncertainties with those reported by (Shi et al. 2022).

$$\gamma = \gamma_0 \left(\frac{V}{V_0} \right)^{q_0} \quad (\text{S.27})$$

$$\theta = \theta_0 \exp \left(\frac{\gamma_0 - \gamma}{q_0} \right) \quad (\text{S.28})$$

Using the high-temperature data reported by (Fiquet et al. 1999; Higo et al. 2018; Shi et al. 2022), the following thermal parameters were obtained: $\gamma_0 = 1.31 \pm 0.01$ and $q_0 = 2.12 \pm 0.18$. The fit quality is shown in Fig. S.3b, by plotting the difference between measured and predicted volume as a function of pressure and temperature. Using a different description of the Grüneisen parameter and the Debye temperature (i.e. equations S.27 and S.28) would yield $\gamma_0 = 1.33 \pm 0.01$ and $q_0 = 1.91 \pm 0.17$.

The fitting parameters are reported in Table S.1. They seem to argue in favor of low values of the bulk modulus and its bulk derivative.

Table S.1: Thermoelastic parameters of alumina from our fit and comparison with literature data

	K_{T0} (GPa)	K'	θ_0 (K)	γ_0	q_0
Fit on literature data	249.7 ± 3.2	3.97 ± 0.10	933 (fixed)	1.31 ± 0.01	2.12 ± 0.18
D'Amour et al. (1978)	254.4 ± 2.0	4.28 ± 0.01			
Dubrovinsky et al. (1998)	258 ± 2	4.88 ± 0.04			
Dewaele and Torrent (2013)	254.1 ± 7.6	4.00 ± 0.15			
Higo et al. (2018) ^a	251.2 ± 1.8	4.21 ± 0.10			
Shi et al. (2022)	246 ± 2	4 (fixed)	1100 (fixed)	1.32 ± 0.07	0.8 ± 0.4
Stixrude and Lithgow-Bertelloni (2011) ^b	253 ± 5	4.3 ± 0.2	933 ± 3	1.32 ± 0.04	1.3 ± 0.2
Oganov and Ono (2005) ^c	252.6	4.24			
Wang and Wu (2018) ^c	258.29	3.94			

^a The bulk modulus value reported here corresponds to the adiabatic bulk modulus K_{S0}

^b This study conducted a global inversion on existing literature data

^c Theoretical studies

S.7 Fitting a p - v_p , v_s -T equation of state from literature and our collected data

Our velocity data on San Carlos-like olivine collected for the BT613 experiment (Table S.2) along with existing literature data were fitted to refine the thermoelastic parameters of olivine of mantle compositions. The fit was conducted iteratively, using the equations described in section S.5. First, elastic stiffness coefficients, c_{ij} , obtained from room temperature Brillouin measurements (Abramson et al., 1997; Mao et al., 2015; Zha et al., 1998; Zhang and Bass, 2016) were inverted into elastic compliance coefficients, s_{ij} , and both tensors were used to calculate the adiabatic bulk modulus and shear modulus following the Voigt (iso-strain) and Reuss (iso-stress) bounds. The Hill average was then calculated by taking the arithmetic mean value of the Voigt and Reuss elastic moduli. From these and density data obtained from the X-ray powder diffraction data collected at the same conditions used for the ultrasonic measurements, K_{T0} , G_0 , K' and G' are fitted using equations S.10, S.12 to S.22, and equation S.26. For the first iteration, the Grüneisen parameter and its volume derivative at ambient conditions, γ_0 and q_0 , are fixed to 1; the Debye temperature is fixed to 809 K, following (Stixrude and Lithgow-Bertelloni 2011). Thermal expansion data at atmospheric pressure (Bouhifd et al., 1996) are then used to fit the Grüneisen parameter by fixing the room temperature Hill average moduli and their pressure derivatives obtained previously, using equations S.8 to S.17. Finally, the volume and shear strain derivative of the Grüneisen parameter, q_0 and η_{S0} , were fitted using our velocity data at high temperatures (equations S.10 and S.12 to S.26).

Table S.2: Temperature, unit cell volume, sample length, and P- and S-wave velocities collected during BT530 and BT613 experiments. As mentioned in the main text and as evidenced in Fig. S.1, the P-wave velocities reported for BT530 are underestimated due to the limited frequency range, they are reported here but were not taken into account to fit elastic parameters. Uncertainties correspond to two standard deviations.

BT613							
Load (bar)	Temperature (K)	Unit cell volumes (\AA^3)			Sample length (μm)	Elastic wave velocities (m.s^{-1})	
		Olivine	MgO	Al_2O_3		P-waves	S-waves
0	300	291.53(3)	74.67(3)	254.59(4)	1507.0(20)	-	-
120	300	271.14(12)	71.24(9)	-	1493.3(144)	9181(90)	5030(50)
120	773	278.38(6)	-	249.73(7)	1511.9(144)	8835(86)	4912(47)
120	1173	285.48(6)	74.15(4)	253.90(8)	1532.5(144)	8589(81)	4792(46)
120	1373	288.65(5)	75.17(3)	255.64(6)	1541.3(144)	8444(80)	4719(44)
120	1473	290.85(4)	75.40(3)	256.58(5)	1547.7(144)	8393(80)	4683(44)
120	1573	292.15(4)	76.01(3)	257.77(4)	1551.5(144)	8282(79)	4603(44)
120	1673	294.78(5)	76.36(3)	259.00(4)	1569.5(144)	8210(76)	4516(44)
120	1573	294.17(4)	76.39(3)	258.66(4)	1569.7(144)	8213(76)	4547(44)
120	1473	293.55(6)	76.16(3)	258.15(4)	1569.1(144)	8253(77)	4561(43)
120	1373	292.73(6)	75.90(3)	257.50(4)	1567.6(144)	8299(79)	4660(44)
120	1273	291.89(4)	75.70(3)	256.93(4)	1565.2(144)	8341(80)	4692(43)
120	1073	290.65(4)	75.15(3)	255.75(4)	1563.2(144)	8422(80)	4782(45)
120	873	289.34(5)	74.77(4)	254.75(4)	1535.2(144) ^a	8350(80)	4729(44)
120	773	288.87(4)	74.53(4)	254.30(4)	1559.9(144)	8527(81)	4832(45)
120	673	288.20(4)	74.34(4)	253.86(4)	1559.2(144)	8564(81)	4863(45)
120	300	286.50(5)	73.68(3)	252.56(4)	1555.9(144)	8673(81)	4964(46)

BT530							
Load (bar)	Temperature (K)	Unit cell volumes (\AA^3)			Sample length (μm)	Elastic wave velocities (m.s^{-1})	
		Olivine	MgO	Al_2O_3		P-waves	S-waves
0	300	291.77(7)	-	254.59(7)	1198.0(20)	-	-

325	673	275.20(7)	-	-	1049.1(144)	8847(123)	4946(68)
325	873	-	-	-	1047.8(144)	8800(126)	4913(68)
325	1073	276.26(7)	-	248.73(7)	1048.8(144)	8782(124)	4882(67)
325	1250	276.76(7)	-	249.41(7)	1049.7(144)	8733(123)	4837(66)
325	1473	278.16(6)	-	250.76(7)	1055.5(144)	8674(118)	4773(65)
325	1573	279.26(7)	-	251.47(7)	1061.8(144)	8623(117)	4720(64)
325	1473	278.81(8)	-	251.01(7)	1065.4(144)	8682(117)	4765(64)
325	1373	278.30(8)	-	250.55(7)	1065.5(144)	8709(118)	4807(65)
325	1273	277.91(7)	-	250.14(7)	1064.9(144)	8734(118)	4834(65)
325	1173	277.51(8)	-	249.72(7)	1064.5(144)	8758(119)	4864(66)
325	773	276.16(7)	-	248.22(6)	1062.4(144)	8832(119)	4964(66)
325	573	275.47(7)	-	247.62(6)	1062.7(144)	8877(120)	5021(68)
325	323	274.90(6)	-	247.10(6)	1062.5(144)	8922(121)	5082(69)
450	300	272.33(7)	-	245.70(5)	1059.4(144)	9037(123)	5118(70)
450	773	273.09(8)	-	246.75(5)	1060.0(144)	8954(122)	4993(68)
450	973	273.52(8)	-	247.34(6)	1061.7(144)	8940(122)	4963(67)
450	1173	273.85(8)	-	247.89(6)	1060.9(144)	8904(121)	4912(67)
450	1373	274.44(9)	-	248.59(6)	1060.7(144)	8868(122)	4875(66)
450	1573	275.28(8)	-	249.54(3)	1060.9(144)	8869(123)	4880(66)

^a The sample length reported here seems to be off compared to the surrounding data points. It appears that the press did not fully rotate back to 0° when the image was taken, resulting in this apparent smaller sample length.

This fitting procedure was repeated iteratively until all parameters converged. The fit quality on literature data is reported in Fig. S.4. Here also, the *integrate* function from the *scipy* python library was used to numerically calculate the integrals involved in equations S.12 and S.23, and the least-squares minimization was conducted using the *curvefit* function, both from the *scipy* python library. The resulting Reuss and Voigt bounds and the Hill average of the isothermal bulk and shear modulus, their pressure derivative, the Grüneisen parameter, and its volume and shear stress derivative are reported in Table S.3. The parameters obtained here are in good agreement with existing global inversions (Stixrude and Lithgow-Bertelloni, 2011, 2005), within uncertainty. The main difference lies in the values of the volume and shear strain derivative of the Grüneisen parameter, which are lower than previously reported.

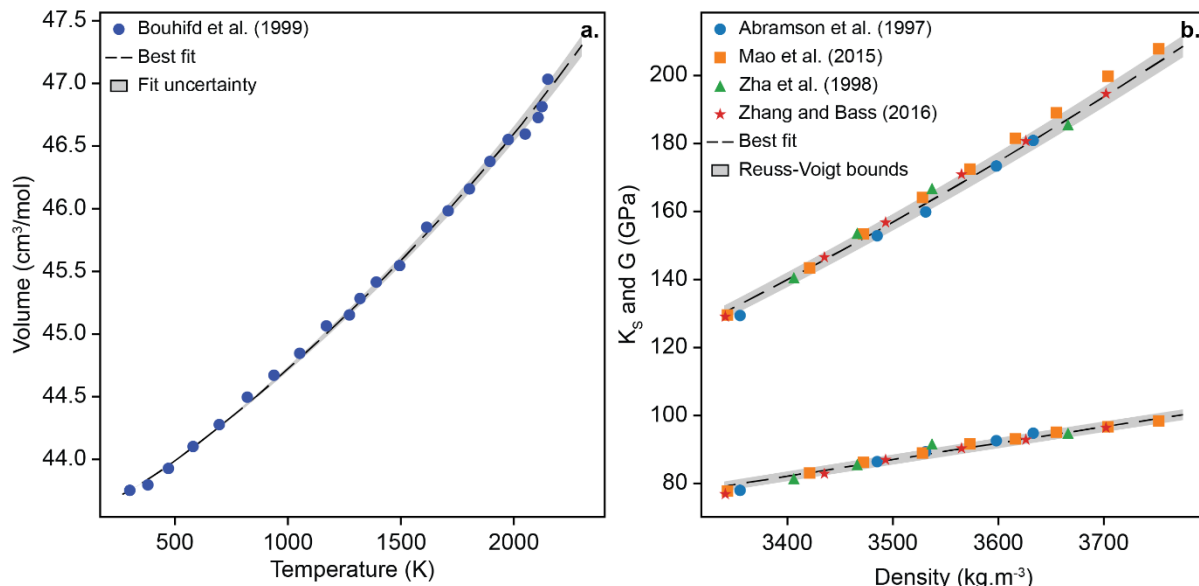


Figure S.4: Plots showing the final fit parameters after converging. (a) Fit of the thermal expansion data (Bouhifd et al., 1996) and (b) fit of the room temperature Brillouin data(Abramson et al., 1997; Mao et al., 2015; Zha et al., 1998; Zhang and Bass, 2016).

Table S.3: Thermoelastic parameters of San Carlos-like olivine and comparison with literature data

Best fit parameters	K_{T0} (GPa)	K'	G_0 (GPa)	G'	γ_0	q_0	θ_0 (K)	η_{S0}
Reuss bound	130.7(26)	4.04(28)	78.6(25)	1.25(24)	1.09(8)	1.61(34)	809 (fixed)	1.65(10)
Voigt bound	134.8(24)	4.03(26)	81.4(24)	1.24(22)	1.09(8)	1.61(34)	809 (fixed)	1.65(10)
Hill average	132.8(24)	4.03(28)	80.0(24)	1.24(24)	1.09(8)	1.61(34)	809 (fixed)	1.65(10)
Angel et al. (2018), Reuss bound	126.3(2)	4.54(6)	-	-	1.044(4)	1.9(2)	644(9)	-
Stixrude et al. (2011), Forsterite composition	128(2)	4.2(2)	82(2)	1.5(1)	0.99(3)	2.1(2)	809(1)	2.3(1)

S.8 Evaluation of uncertainties

Uncertainties associated with the P- and S-wave travel times are expected to affect the uncertainties on the pressure determined using our dual travel time method. To predict this effect, the uncertainties on the travel times were propagated using a Monte Carlo random throw simulation, and the results are reported in Fig. 5. As Fig. 5a corresponds to a purely synthetic exercise, the average typical uncertainties on the collected travel times were considered. Based on our travel time data, the average relative uncertainty associated with P-waves is 0.4 % and that associated with S-waves is 0.2 %. Note that these relative uncertainties were kept constant for the different materials investigated. The errors were assumed to follow a Gaussian distribution, and, for each point, 10^4 random sets of P- and S-wave travel times were generated. Thus 10^4 S- to P-wave travel time ratios can be predicted, yielding as many pressure values. The reported uncertainty on pressure (shaded areas in Fig. 5a) was thus considered to be two times the standard deviation of these 10^4 pressure values.

A similar Monte Carlo simulation was conducted to estimate the uncertainties of the estimated pressure values, based on the travel time data collected during BT613. The error distribution was assumed to be Gaussian. For each temperature step, 10^4 random sets of P- and S-wave travel times were predicted within one standard deviation of the collected travel times at various frequencies, yielding 10^4 travel time ratios. For each ratio, the EoS is solved to determine pressure, and the uncertainty on pressure is considered to correspond to two standard deviations of the 10^4 pressure values. These two standard deviations correspond to the vertical bars reported in Fig. 5b. For the sake of clarity and as the uncertainties associated with the dual travel time method are temperature dependent, only these were reported for each data point. The uncertainties associated with pressure values determined from X-ray diffraction are reported in the legend as the average uncertainty. These uncertainties are also evaluated through a Monte Carlo where the error distribution is once more assumed to be Gaussian. For each volume collected, 10^4 random unit cell volumes along 10^4 random sets of EoS parameters are generated within uncertainties. For each set, a pressure value of the EoS is solved to yield a value of pressure. The uncertainty is thus taken to correspond to two standard deviations of the 10^4 pressure values obtained for each volume. Interestingly, the errors associated with the pressure determined from X-ray diffraction are extremely similar, irrespective of the material or temperature, and correspond to ± 0.4 GPa.

References

- Abramson, E.H., Brown, J.M., Slutsky, L.J., Zaug, J., 1997. The elastic constants of San Carlos olivine to 17 GPa. *J Geophys Res Solid Earth* 102, 12253–12263. <https://doi.org/10.1029/97JB00682>
- Angel, R.J., Alvaro, M., Nestola, F., 2018. 40 Years of Mineral Elasticity: a Critical Review and a New Parameterisation of Equations of State for Mantle Olivines and Diamond Inclusions. *Physics and Chemistry of Minerals* 45, 95–113. <https://doi.org/10.1007/s00269-017-0900-7>
- Birch, F., 1952. Elasticity and constitution of the Earth's interior. *Journal of Geophysical Research* 57, 227–286. <https://doi.org/10.1029/JZ057i002p00227>
- Bouhifd, M.A., Andrault, D., Fiquet, G., Richet, P., 1996. Thermal expansion of forsterite up to the melting point. *Geophys Res Lett.* <https://doi.org/10.1029/96GL01118>
- D'Amour, H., Schiferl, D., Denner, W., Schulz, H., Holzapfel, W.B., 1978. High-pressure single-crystal structure determinations for ruby up to 90 kbar using an automatic diffractometer. *Journal of Applied Physics* 49, 4411–4416. <https://doi.org/10.1063/1.325494>
- Dewaele, A., Torrent, M., 2013. Equation of state of α -Al₂O₃. 064107, 1–5. <https://doi.org/10.1103/PhysRevB.88.064107>
- Dubrovinsky, L.S., Saxena, S.K., Lazor, P., 1998. High-pressure and high-temperature in situ X-ray diffraction study of iron and corundum to 68 GPa using an internally heated diamond anvil cell. *Physics and Chemistry of Minerals* 25, 434–441. <https://doi.org/10.1007/s002690050133>
- Fiquet, G., Richet, P., Montagnac, G., 1999. High-temperature thermal expansion of lime, periclase, corundum and spinel. *Physics and Chemistry of Minerals* 27, 103–111. <https://doi.org/10.1007/s002690050246>
- Higo, Y., Irfune, T., Funakoshi, K.I., 2018. Simultaneous high-pressure high-temperature elastic velocity measurement system up to 27 GPa and 1873 K using ultrasonic and synchrotron X-ray techniques. *Review of Scientific Instruments* 89. <https://doi.org/10.1063/1.4993121>
- Keppler, H., Frost, D.J., 2005. Introduction to minerals under extreme conditions, in: *Mineral Behaviour at Extreme Conditions*. Mineralogical society of Great Britain and Ireland, London, pp. 1–30. <https://doi.org/10.1180/EMU-notes.7.1>
- Mao, Z., Fan, D., Lin, J.-F., Yang, J., Tkachev, S.N., Zhuravlev, K., Prakapenka, V.B., 2015. Elasticity of single-crystal olivine at high pressures and temperatures. *Earth Planet Sci Lett* 426, 204–215. <https://doi.org/10.1016/j.epsl.2015.06.045>
- Oganov, A.R., Ono, S., 2005. The high-pressure phase of alumina and implications for Earth's D'' layer. *Proceedings of the National Academy of Sciences of the United States of America* 102, 10828–10831. <https://doi.org/10.1073/pnas.0501800102>
- Richet, P., Xu, J.A., Mao, H.K., 1988. Quasi-hydrostatic compression of ruby to 500 Kbar. *Physics and Chemistry of Minerals* 16, 207–211. <https://doi.org/10.1007/BF00220687>
- Shi, W., Wei, W., Sun, N., Mao, Z., Prakapenka, V.B., 2022. Thermal Equations of State of Corundum and Rh₂O₃ (II)-Type Al₂O₃ up to 153 GPa and 3400 K. *Journal of Geophysical Research: Solid Earth* 127. <https://doi.org/10.1029/2021JB023805>
- Stixrude, L., Lithgow-Bertelloni, C., 2011. Thermodynamics of mantle minerals - II. Phase equilibria. *Geophys J Int* 184, 1180–1213. <https://doi.org/10.1111/j.1365-246X.2010.04890.x>
- Stixrude, L., Lithgow-Bertelloni, C., 2005. Thermodynamics of mantle minerals - I. Physical properties. *Geophys J Int* 162, 610–632. <https://doi.org/10.1111/j.1365-246X.2005.02642.x>
- Tange, Y., Nishihara, Y., Tsuchiya, T., 2009. Unified analyses for P-V-T equation of state of MgO: A solution for pressure-scale problems in high P-T experiments. *J Geophys Res Solid Earth* 114, 1–16. <https://doi.org/10.1029/2008jb005813>
- Toby, B.H., Von Dreele, R.B., 2013. GSAS-II: the genesis of a modern open-source all purpose crystallography software package. *J Appl Crystallogr* 46, 544–549. <https://doi.org/10.1107/S0021889813003531>

- Wang, W., Wu, Z., 2018. Elasticity of Corundum at High Pressures and Temperatures: Implications for Pyrope Decomposition and Al-Content Effect on Elastic Properties of Bridgmanite. *Journal of Geophysical Research: Solid Earth* 123, 1201–1216. <https://doi.org/10.1002/2017JB015088>
- Zha, C., Duffy, T.S., Downs, R.T., Mao, H., Hemley, R.J., 1998. Brillouin scattering and X-ray diffraction of San Carlos olivine: direct pressure determination to 32 GPa. *Earth Planet Sci Lett* 159, 25–33. [https://doi.org/10.1016/S0012-821X\(98\)00063-6](https://doi.org/10.1016/S0012-821X(98)00063-6)
- Zhang, J.S., Bass, J.D., 2016. Sound velocities of olivine at high pressures and temperatures and the composition of Earth's upper mantle. *Geophys Res Lett* 43, 9611–9618. <https://doi.org/10.1002/2016GL069949>